



CHORUS

This is the accepted manuscript made available via CHORUS. The article has been published as:

Antiferromagnetism in semiconducting $\text{SrMn}_{\{2\}}\text{Sb}_{\{2\}}$ and $\text{BaMn}_{\{2\}}\text{Sb}_{\{2\}}$ single crystals

N. S. Sangeetha, V. Smetana, A.-V. Mudring, and D. C. Johnston

Phys. Rev. B **97**, 014402 — Published 3 January 2018

DOI: [10.1103/PhysRevB.97.014402](https://doi.org/10.1103/PhysRevB.97.014402)

Antiferromagnetism in semiconducting SrMn_2Sb_2 and BaMn_2Sb_2 single crystals

N. S. Sangeetha,¹ V. Smetana,² A.-V. Mudring,² and D. C. Johnston^{1,3}

¹*Ames Laboratory, Iowa State University, Ames, Iowa 50011, USA*

²*Department of Materials and Environmental Chemistry,*

Stockholm University, Svante Arrhenius väg 16 C, 106 91 Stockholm, Sweden

³*Department of Physics and Astronomy, Iowa State University, Ames, Iowa 50011, USA*

(Dated: December 13, 2017)

Crystals of SrMn_2Sb_2 and BaMn_2Sb_2 were grown using Sn flux and characterized by powder and single-crystal x-ray diffraction, respectively, and by single-crystal electrical resistivity ρ , heat capacity C_p , and magnetic susceptibility χ measurements versus temperature T , and magnetization versus field $M(H)$ isotherm measurements. SrMn_2Sb_2 adopts the trigonal CaAl_2Si_2 -type structure whereas BaMn_2Sb_2 crystallizes in the tetragonal ThCr_2Si_2 -type structure. The $\rho(T)$ data indicate semiconducting behaviors for both compounds with activation energies of ≥ 0.35 eV for SrMn_2Sb_2 and 0.16 eV for BaMn_2Sb_2 . The $\chi(T)$ and $C_p(T)$ data reveal antiferromagnetic (AFM) ordering at $T_N = 110$ K for SrMn_2Sb_2 and 450 K for BaMn_2Sb_2 . The anisotropic $\chi(T \leq T_N)$ data also show that the ordered moments in SrMn_2Sb_2 are aligned in the hexagonal ab plane whereas the ordered moments in BaMn_2Sb_2 are aligned collinearly along the tetragonal c axis. The ab -plane $M(H)$ data for SrMn_2Sb_2 exhibit a continuous metamagnetic transition at low fields $0 < H \lesssim 1$ T, whereas BaMn_2Sb_2 exhibits no metamagnetic transitions up to 5.5 T. The $\chi(T)$ and $C_p(T)$ data for both SrMn_2Sb_2 and BaMn_2Sb_2 indicate strong dynamic short-range AFM correlations above their respective T_N up to at least 900 K within a local-moment picture, corresponding to quasi-two-dimensional magnetic behavior. The present results and a survey of the literature for Mn pnictides with the CaAl_2Si_2 and ThCr_2Si_2 crystal structures show that the T_N values for the CaAl_2Si_2 -type compounds are much smaller than those for the ThCr_2Si_2 -type materials.

I. INTRODUCTION

The discoveries of high- T_c superconductivity in layered iron pnictides and chalcogenides since 2008 revealed Fe-based materials to be a rich source of unconventional superconductors. In marked contrast to high- T_c layered cuprates, the undoped ferropnictides are metallic and show itinerant antiferromagnetic (AFM) spin-density wave and coincident or nearly coincident structural transitions. The suppression of these transitions by chemical doping resulted in superconductivity in the “1111”-type parent compound LaFeAsO with $T_c = 26$ K in 2008¹. Since then, many compounds with related layered crystal structures and chemical compositions were discovered which are classified as “11”-type (e.g. binary iron chalcogenide FeSe), “111”-type (e.g. ternary LiFeAs or NaFeAs), 1111-type with the primitive-tetragonal ZrCuSiAs -type structure with space group $P4/nmm$ (e.g. RFeAsO , $R = \text{rare earth}$), “122”-type with the body-centered tetragonal ThCr_2Si_2 structure with space group $I4/mmm$ (e.g. AFe_2As_2 , $A = \text{Ca, Sr, Ba, Eu}$), and other related structures^{2–5}. The highest reported T_c for a bulk Fe-based superconductor is 56 K for $\text{Gd}_{0.8}\text{Th}_{0.2}\text{FeAsO}$ ⁶.

In attempts to further enhance the T_c of such superconductors and search for other exotic ground states, additional isostructural compounds based on other transition metals in place of Fe including Cr, Mn, Co, and Ni have been studied. These pnictides include metallic Co-based^{7–15}, itinerant AFM Cr-based^{16–24}, semiconducting AFM Mn-based^{25–33} and superconducting Ni-based^{34–37} compounds.

Semiconducting layered quasi-two-dimensional AFM Mn pnictides received special attention as potential parent compounds for superconductivity because they could form a bridge between the superconducting iron-arsenide and cuprate families of high- T_c materials. The 1111-type LaMnPO and 122-type BaMn_2As_2 have been most extensively studied. These compounds exhibit insulator (at temperature $T = 0$) to metal transitions either upon doping or application of pressure, but no superconductivity in these compounds has been observed. The AFM ordering (Néel) temperature T_N , ordered moment μ at low T , and activation energy Δ have been reported for several semiconducting 1111-type Mn pnictides, including LaMnPO ³¹, LaMnAsO ³², and LaMnSbO ³³, as summarized in Table I for these compounds and also for those below. They tend to have a simple checkerboard (G-type) AFM structure, indicating stronger ab -plane nearest-neighbour (NN) exchange interactions J_1 compared to twice the next-nearest-neighbor interactions J_2 , i.e., $J_1 > 2J_2$ ³. A high-pressure measurement on LaMnPO showed a semiconductor to metal transition at a pressure of 10 GPa³⁸. Fluorine-doped $\text{LaMnPO}_{1-x}\text{F}_x$ also exhibits an insulator to metal transition on doping which only weakly affects T_N and μ ³⁹, similar to $\text{La}_{1-x}\text{Sr}_x\text{MnAsO}$ ⁴⁰. On the other hand, hydrogen- and deuterium-substituted $\text{LaMnAsO}_{1-x}(\text{H/D})_x$ exhibits insulator to metal transitions associated with the emergence of itinerant ferromagnetism⁴¹.

The 122-type BaMn_2X_2 compounds with the ThCr_2Si_2 -type structure containing $X = \text{P, As, or Bi}$ have also been extensively studied. BaMn_2P_2 ²⁵, BaMn_2As_2 ^{26,42}, and BaMn_2Bi_2 ^{29,43} undergo G-type

AFM ordering with the ordered moments aligned along the c axis, where the NN exchange interactions J_1 are again dominant. A high-pressure study of BaMn_2As_2 showed an insulator to metal transition at 5.8 GPa with a downturn in the resistivity below ~ 17 K and no change in the crystal structure⁴⁴. Interestingly, substitution of only 1.6% of K for Ba results in a metallic ground state in BaMn_2As_2 ⁴⁵. Furthermore, itinerant FM occurs in $\text{Ba}_{1-x}\text{K}_x\text{Mn}_2\text{As}_2$ with $x = 0.19$ and 0.26 ⁴⁶ and half-metallic FM behavior is found below the Curie temperature $T_C \approx 100$ K for 40% K-doped⁴⁷ and 60% Rb-doped BaMn_2As_2 ⁴⁸. This itinerant FM⁴⁹ is aligned in the ab plane and coexists with the G-type local-moment AFM of the Mn spins aligned along the c axis⁵⁰. Similar to BaMn_2As_2 , the isostructural AFM semiconductor BaMn_2Bi_2 exhibits metallic behavior with K doping and the magnetic character of $\text{Ba}_{1-x}\text{K}_x\text{Mn}_2\text{Bi}_2$ up to 36% K doping is inferred to be local-moment AFM²⁹.

Interestingly, unlike body-centered tetragonal 122-type $\text{BaMn}_2(\text{P}, \text{As}, \text{Sb}, \text{Bi})_2$, the 122-type $(\text{Ca}, \text{Sr})\text{Mn}_2(\text{P}, \text{As}, \text{Sb}, \text{Bi})_2$ compounds crystallize in the trigonal CaAl_2Si_2 -type structure with space group $P\bar{3}m1$. Empirically, the CaAl_2Si_2 -type structure is found if the transition metal has a d^0 , d^5 , or d^{10} electronic configuration whereas the ThCr_2Si_2 -type structure has no such preferences. The Mn sublattice can be viewed either as a corrugated honeycomb layer or a triangular-lattice bilayer which suggests the possibility of geometric frustration. Some of these trigonal compounds are known to be AFM semiconductors: SrMn_2P_2 ²⁵, CaMn_2As_2 ³⁰, SrMn_2As_2 ^{30,51}, CaMn_2Sb_2 ^{52–54}, and CaMn_2Bi_2 ⁵⁵.

The compounds in Table I also manifest strong dynamic short-range AFM correlations at $T \gg T_N$, similar to BaMn_2As_2 ⁵⁶. Neutron diffraction studies of both CaMn_2Sb_2 and CaMn_2Bi_2 revealed a collinear AFM structure with the ordered moments aligned in the ab plane^{55,57}. However, whereas one neutron structural study of CaMn_2Sb_2 concluded that collinear AFM moments are aligned in the ab plane⁵³, another suggested that the collinear ordered moments are canted by 25° with respect to the ab plane⁵². Single-crystal neutron diffraction measurements on trigonal SrMn_2As_2 showed that the Mn moments are ordered in the ab plane in a collinear Néel AFM structure below $T_N = 118(2)$ K⁵¹ and magnetic susceptibility data exhibited quasi-2D behavior at $T \gg T_N$ ³⁰, as does ThCr_2Si_2 -type BaMn_2As_2 as noted above. SrMn_2P_2 exhibits a novel pressure-induced structural transition from the trigonal CaAl_2Si_2 -type to the body-centered tetragonal ThCr_2Si_2 -type structure⁵⁸.

In order to extend the above work on the Mn pnictides and attempt to discover new properties, herein we report the growth, crystal structure, $\rho(T)$, magnetization versus applied magnetic field $M(H)$ isotherms, $\chi(T)$ and heat capacity $C_p(T)$ measurements of BaMn_2Sb_2 , which crystallizes in the ThCr_2Si_2 -type structure⁵⁹, and SrMn_2Sb_2 which has the CaAl_2Si_2 -type structure⁶⁰. Since the Mn sublattice in SrMn_2Sb_2 is a corrugated honeycomb or

TABLE I: Properties of 1111-type and 122-type Mn pnictides, including results from the present work (PW). Included are the structure type, AFM ordering temperatures T_N , low-temperature ordered moment μ , and semiconducting activation energy Δ . The ZrCuSiAs structure is primitive tetragonal with space group $P4/nmm$, the ThCr_2Si_2 structure is body-centered tetragonal with space group $I4/mmm$, and the CaAl_2Si_2 structure is trigonal with space group $P\bar{3}m1$. Unless otherwise indicated, Δ was determined from electrical resistivity data with the current in the crystallographic ab plane of single-crystal samples.

Compound	Structure Type	T_N (K)	μ (μ_B/Mn)	Δ (eV)	Ref.
1111-type					
LaMnPO	ZrCuSiAs	375	2.26		31
LaMnAsO	ZrCuSiAs	360	3.33		32
LaMnSbO	ZrCuSiAs	255	3.45		33
122-type					
BaMn_2P_2	ThCr_2Si_2		4.2	0.073	^{25a}
BaMn_2As_2	ThCr_2Si_2	625	3.88	0.027	^{26,42}
BaMn_2Sb_2	ThCr_2Si_2			1.12 ^b	28
BaMn_2Sb_2	ThCr_2Si_2	450		0.16	PW
BaMn_2Bi_2	ThCr_2Si_2	400	3.83	0.003	^{29,43}
CaMn_2As_2	CaAl_2Si_2	62		0.061	³⁰
CaMn_2Sb_2	CaAl_2Si_2	85–88	3.46		^{52–54}
CaMn_2Bi_2	CaAl_2Si_2	150	3.85	0.031	⁵⁵
SrMn_2P_2	CaAl_2Si_2	53		0.013	^{25a}
SrMn_2As_2	CaAl_2Si_2	120	3.6	0.085	^{30,51}
SrMn_2Sb_2	CaAl_2Si_2	110		≥ 0.35	PW

^aPolycrystalline sample.

^bMeasured at 470–773 K.

triangular bilayer sublattice whereas the Mn sublattice in BaMn_2Sb_2 is a stacked square lattice, the difference in the geometry of Mn network between BaMn_2Sb_2 and SrMn_2Sb_2 may be important to take into account when comparing their properties.

Previous theoretical electronic structure studies on BaMn_2Sb_2 suggested a G-type AFM ordering^{61,62}, but T_N and the AFM structure have not been experimentally determined. Transport measurements revealed that BaMn_2Sb_2 has a room-temperature Seebeck coefficient of ~ 225 $\mu\text{V}/\text{K}$, consistent with semiconducting behavior. With regard to SrMn_2Sb_2 , a polycrystalline sample showed “complex magnetic ordering of the Mn moments below ≈ 265 K” and $\rho(T)$ measurements on a crystal suggested a “metallic-like temperature dependence”⁶³. However, in contradiction to both of these results, the present study on SrMn_2Sb_2 crystals reveals AFM ordering at $T_N = 110$ K with an insulating ground state.

The remainder of the paper is organized as follows. Following the experimental details in Sec. II, our structural data are given in Sec. III A. The $\rho(T)$ data for BaMn_2Sb_2 and SrMn_2Sb_2 crystals are presented in

Sec. III B. Our studies of $M(H)$ and $\chi(T)$ for these crystals are presented in Sec. III C. We suggest in Secs. III B and III C 1 the probable origins of the erroneous experimental $\rho(T)$ and $\chi(T)$ results reported in Ref.⁶³, respectively. The $C_p(T)$ measurements on SrMn_2Sb_2 and BaMn_2Sb_2 are presented in Sec. III D, and a summary is given in Sec. IV.

II. EXPERIMENTAL DETAILS

Single crystals of BaMn_2Sb_2 and SrMn_2Sb_2 were grown in Sn flux. High-purity elements Sr (99.99%) and Ba (99.99%) from Sigma Aldrich, and Mn (99.95%), Sb (99.9999%), and Sn (99.999%) from Alfa Aesar, were weighed out in the molar ratio (Ba, Sr):Mn:Sb:Sn = 1.05:2:2:20 and placed in an alumina crucible that was sealed under an Ar pressure of $\approx 1/4$ atm in a silica tube. Excess Sr or Ba was used in the syntheses to avoid the formation of MnSb and thus to assure the formation of magnetically pure samples. After preheating the mixture at 600 °C for 7 h, the assembly was heated to 1150 °C at a rate of 50 °C/h and held at this temperature for 15 h for homogenization. Then the furnace was slowly cooled at a rate of 4 °C/h to 700 °C. Shiny platelike and hexagon-shaped single crystals of BaMn_2Sb_2 and SrMn_2Sb_2 , respectively, were obtained after decanting the Sn flux using a centrifuge. Subsequent handling of the crystals was carried out in a dry box and exposure of them to air during transfer to measurement instruments was kept to a minimum.

Semiquantitative chemical analyses of the single crystals were performed using a JEOL scanning electron microscope (SEM) equipped with an EDX (energy-dispersive x-ray analysis) detector, where a counting time of 120 s was used. A room-temperature powder x-ray diffraction (XRD) pattern was recorded on crushed single crystals of SrMn_2Sb_2 using a Rigaku Geigerflex powder diffractometer with Cu $K\alpha$ radiation ($\lambda = 1.5418$ Å) at diffraction angles 2θ from 10° to 110° with a 0.02° step width. The data were analysed by Rietveld refinement using FullProf software⁶⁴.

Single-crystal x-ray structural analysis of BaMn_2Sb_2 was performed at room temperature using a Bruker D8 Venture diffractometer equipped with a Photon 100 CMOS detector, a flat graphite monochromator and a Mo $K\alpha$ $I\mu\text{S}$ microfocus x-ray source ($\lambda = 0.71073$ Å) operating at a voltage of 50 kV and a current of 1 mA. The raw frame data were collected using the Bruker APEX3 program⁶⁵, while the frames were integrated with the Bruker SAINT software package⁶⁶ using a narrow-frame algorithm integration of the data and were corrected for absorption effects using the multiscan method (SADABS)⁶⁷. The atomic thermal factors were refined anisotropically. Initial models of the crystal structures were first obtained with the program SHELXT-2014⁶⁸ and refined using the program SHELXL-2014⁶⁹ within the APEX3 software package.

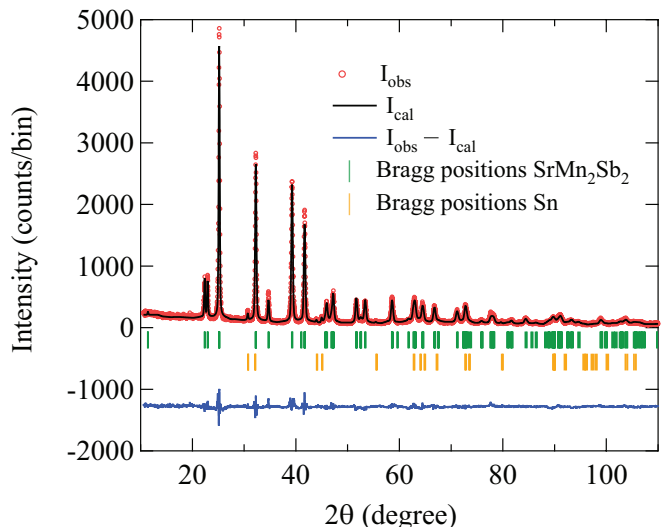


FIG. 1: (Colour online) Powder x-ray diffraction patterns (open circles) of SrMn_2Sb_2 at room temperature. Shown are the observed intensity data (I_{obs} , open red circles), the Rietveld refinement fit calculated for the CaAl_2Si_2 -type trigonal structure with space group $P3m1$ together with small amounts of adventitious elemental Sn impurity on the crystal surfaces from the Sn flux (I_{cal} , solid blue curve through the data), the difference $I_{\text{obs}} - I_{\text{cal}}$ (bottom blue plot), and the Bragg peak positions for SrMn_2Sb_2 (vertical green tick marks) and Sn (vertical orange tick marks).

Magnetization M versus temperature T measurements at fixed field over the T range $1.8 \leq T \leq 350$ K and M versus applied field H isotherm measurements for $H \leq 5.5$ T were carried out using a Quantum Design, Inc., Magnetic Properties Measurement System (MPMS). The high-temperature $M(T)$ for $300 \text{ K} \leq T \leq 900$ K was measured using the vibrating-sample magnetometer (VSM) option of a Quantum Design, Inc., Physical Properties Measurement System (PPMS). Four-probe dc $\rho(T)$ and $C_p(T)$ measurements were carried out on the PPMS, where electrical contacts to a crystal for the $\rho(T)$ measurements were made using annealed 0.05 mm diameter Pt wires and silver epoxy.

III. EXPERIMENTAL RESULTS

A. Crystal Structures

SEM images of the crystal surfaces indicated single-phase crystals. EDX analyses of the chemical compositions were in agreement with the expected 1:2:2 stoichiometry of the compounds and the amount of Sn incorporated into the crystal structure from the Sn flux is zero to within experimental error.

Powder XRD data on crushed SrMn_2Sb_2 single crystals confirmed their single-phase nature. The Rietveld refinement of the XRD pattern is shown in Fig. 1, confirming

TABLE II: Refined crystallographic parameters obtained from XRD of SrMn₂Sb₂ and BaMn₂Sb₂ crystals. The atomic coordinates in SrMn₂Sb₂ in hexagonal notation are Sr: 1a (0, 0, 0); Mn: 2d (1/3, 2/3, z_{Mn}); and Sb: 2d (1/3, 2/3, z_{Sb}). The atomic coordinates in BaMn₂Sb₂ are Ba: 1a (0, 0, 0); Mn: 2d (0, 1/2, 1/4); and Sb: 2d (0, 0, z_{Sb}). The shortest Mn-Mn interatomic distances in SrMn₂Sb₂ and BaMn₂Sb₂ [see Fig. 2] are also listed.

	SrMn ₂ Sb ₂	BaMn ₂ Sb ₂
Structure	CaAl ₂ Si ₂ -type trigonal	ThCr ₂ Si ₂ -type tetragonal
Space group	$P\bar{3}m1$	$I4/mmm$
Lattice parameters		
a (Å)	4.5888(2)	4.397(4)
c (Å)	7.7529(4)	14.33(2)
c/a	1.6895(2)	3.259(8)
V_{cell} (Å ³)	141.38(1)	277.15(6)
Atomic coordinates		
z_{Mn}	0.62123(12)	
z_{Sb}	0.26133(20)	0.3642(1)
Shortest Mn-Mn distances (Å)		
d_1	3.2471(7)	3.2140(3)
d_2	4.5965(3)	4.4180(6)
d_3	5.6277(5)	6.2480(6)
d_{z1}	6.4753(12)	7.2010(2)
d_{z2}	7.778(2)	14.4020(3)

that SrMn₂Sb₂ has the trigonal CaAl₂Si₂-type structure. Weak peaks from adventitious Sn from the flux are also visible and were refined together with the main phase. The crystallographic parameters of SrMn₂Sb₂ are listed in Table II. The hexagonal lattice parameters a and c obtained are in good agreement with previously reported values^{60,63}.

Single-crystal XRD measurements on BaMn₂Sb₂ confirmed the single-phase nature of the compound and the ThCr₂Si₂-type crystal structure. The crystallographic parameters are listed in Table II. The lattice parameters a and c are in good agreement with the previous values⁵⁹.

Figures 2(a) and 2(c) show perspective views of the unit cells of BaMn₂Sb₂ (tetragonal ThCr₂Si₂-type) and SrMn₂Sb₂ (trigonal CaAl₂Si₂-type), respectively. Both structures look similar in the way they are composed of Mn-Sb tetrahedra separated by Sr/Ba layers. The primary difference between them is the geometry of the Mn layers. In BaMn₂Sb₂, the Mn network is square planar where each Mn atom is coordinated by four Mn atoms at a 90° angle between them as shown in Fig. 2(b). In SrMn₂Sb₂, the planar Mn network can be considered to be either a corrugated Mn honeycomb layer or a double triangular-lattice layer as shown in Fig. 2(d). The dif-

ference between the structures of the Mn layers in the two compounds may be expected to have a significant influence on their physical properties.

The three smallest Mn-Mn intralayer distances d_1 , d_2 , and d_3 and the smallest Mn-Mn interlayer distances d_{z1} and d_{z2} are shown by arrows in Figs. 2(a) and 2(c) for BaMn₂Sb₂ and SrMn₂Sb₂, respectively. These distances are listed in Table II.

B. In-Plane Electrical Resistivity

Figures 3(a) and 3(b) show the ab -plane $\rho(T)$ for BaMn₂Sb₂ and SrMn₂Sb₂, respectively. For both compounds, ρ first increases slowly with decreasing T below 400 K, but then ρ increases rapidly with decreasing T below 300 K. The data clearly indicate that both BaMn₂Sb₂ and SrMn₂Sb₂ have insulating ground states. We fitted the $\rho(T)$ data over restricted temperature intervals by

$$\log_{10} \rho(T) = A + 0.4343 \left(\frac{\Delta}{k_{\text{B}}T} \right), \quad (1)$$

where A is a constant, k_{B} is Boltzmann's constant and Δ is the activation energy.

Plots of $\log_{10} \rho$ vs $1/T$ are shown in the insets of Figs. 3(a) and 3(b) for BaMn₂Sb₂ and SrMn₂Sb₂, respectively. For BaMn₂Sb₂, the data between 1) 240 K and 400 K and between 2) 80 K and 140 K are nearly linear in T and were separately fitted by Eq. (1), yielding the intrinsic and extrinsic activation energies $\Delta_1 = 0.16$ eV and $\Delta_2 = 0.018$ eV, respectively, corroborating previous results²⁸. The fits are shown as the solid straight lines in the inset of Fig. 3(a), and the extrapolations as dashed lines. The fitted activation energies are listed in the inset and Table I and are of the same order as found previously for isostructural BaMn₂P₂²⁵ and BaMn₂As₂²⁶.

In the case of SrMn₂Sb₂, there was no extended region of the $\ln \rho$ versus $1/T$ plot that showed linear behavior, so the data between 340 K and 400 K were fitted by Eq (1), yielding the lower limit to the intrinsic activation energy as $\Delta = 0.35$ eV as shown in the inset and Table I. The fit is shown as the solid straight line in the inset of Fig. 3(b) and the extrapolations by dashed lines.

Our results for SrMn₂Sb₂ contradict a previous report⁶³ where it was claimed that their Sn-flux-grown SrMn₂Sb₂ crystals exhibit a “metallic-like” in-plane $\rho(T)$. In particular, the $\rho(T)$ in Fig. 6 of Ref.⁶³ increases almost linearly from ≈ 30 mΩ cm at low T to ≈ 100 mΩ cm at $T = 300$ K. These values are too large for a metallic layered pnictide³. Furthermore, the intrinsic $\rho(T)$ values in Fig. 3(b) over the same T range are orders of magnitude larger than in Ref.⁶³. We therefore suggest that the origin of these discrepancies is the presence of metallic Sn inclusions in the crystal measured in Ref.⁶³ which would short-circuit the much higher intrinsic resistance of the crystal and lead to their observed T dependence of ρ . We note that the lowest temperature

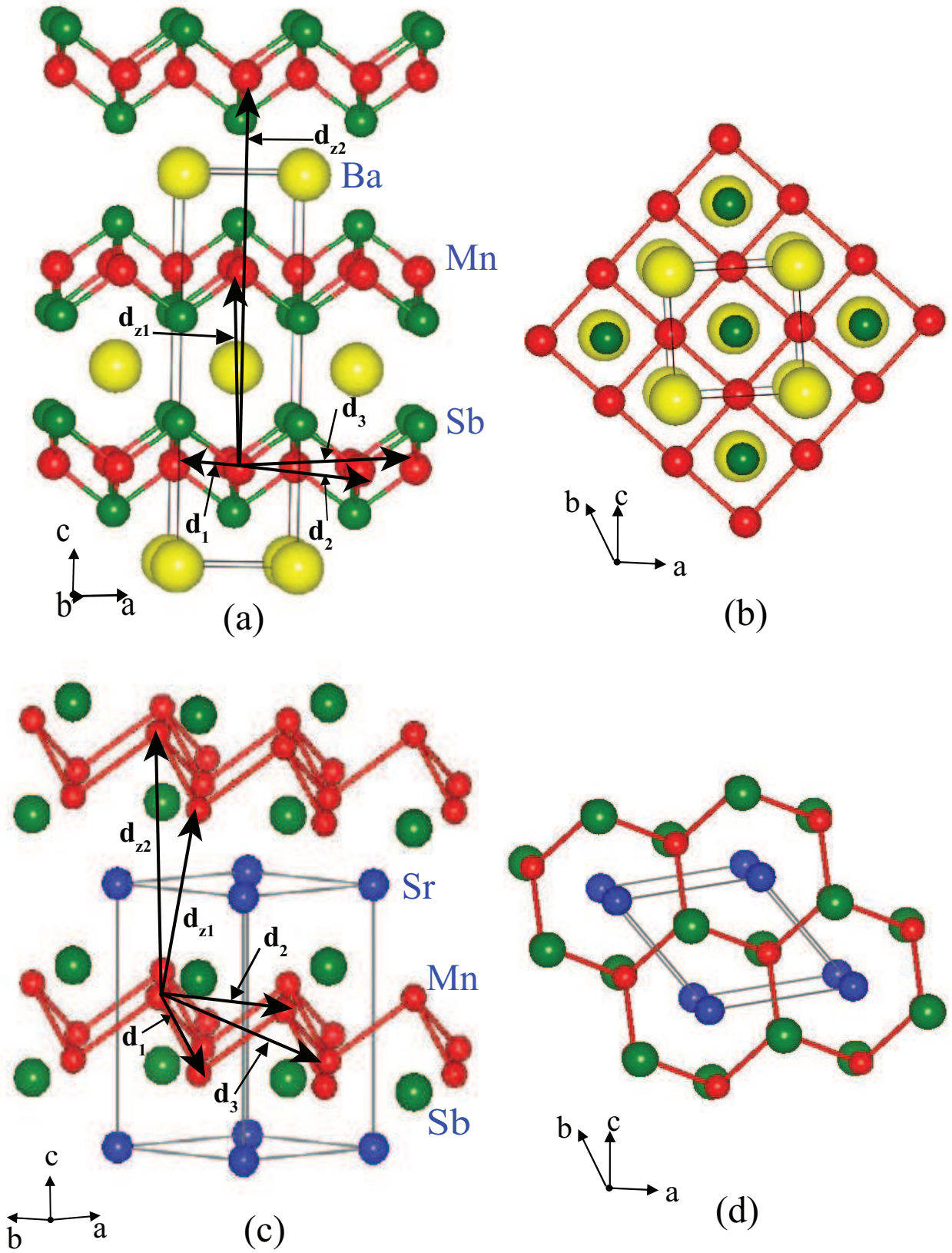


FIG. 2: (Colour online) Outlines of the unit cells of (a) BaMn_2Sb_2 ($I4/mmm$, ThCr₂Si₂-type) and (c) SrMn_2Sb_2 ($P\bar{3}m1$, CaAl₂Si₂-type). The smallest Mn-Mn interatomic distances within the Mn layer (d_1 , d_2 and d_3) and between layers (d_{z1} and d_{z2}) are indicated by arrows. The projections of the manganese networks onto the ab plane with a slight c -axis tilt are shown in (b) BaMn_2Sb_2 (square net) and (d) SrMn_2Sb_2 (corrugated honeycomb net or triangular bilayer).

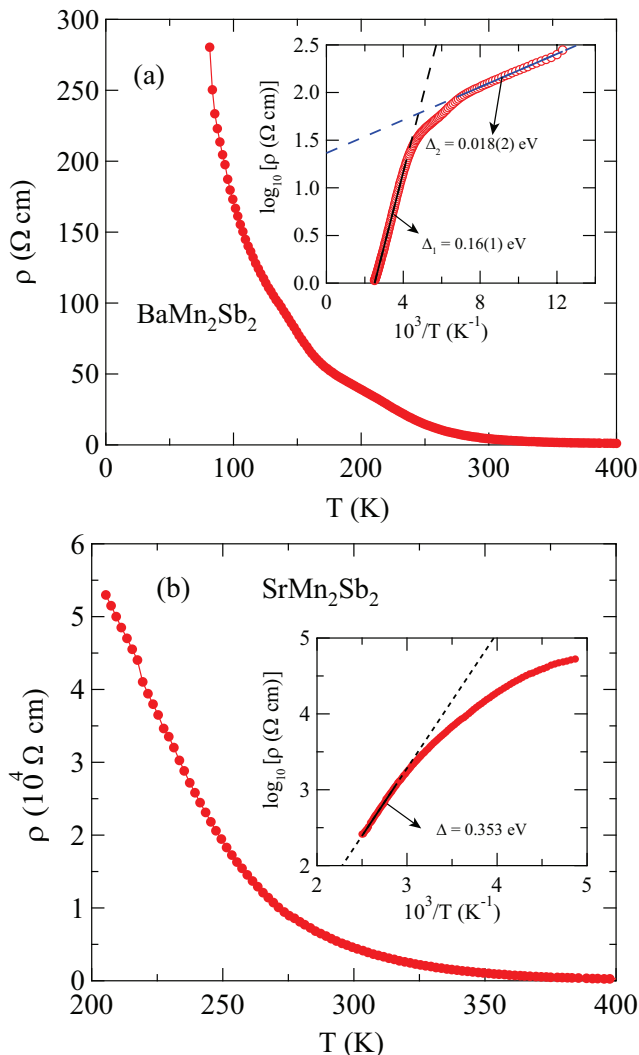


FIG. 3: (Colour online) Temperature T dependence of the electrical resistivity, $\rho(T)$, in the ab plane for (a) BaMn_2Sb_2 and (b) SrMn_2Sb_2 . The insets show plots of $\log_{10} \rho$ versus $1/T$. The solid straight lines through the inset data are fits over restricted temperature intervals by Eq. (1) as discussed in the text, and the dashed lines are extrapolations.

of the $\rho(T)$ measurement in the inset to Fig. 6 of Ref.⁶³ was 4.5 K, just above the superconducting $T_c = 3.7$ K of Sn metal which would likely have been detected by extending their $\rho(T)$ measurement to somewhat lower T .

C. Magnetization and Magnetic Susceptibility

1. SrMn_2Sb_2

Figure 4(a) shows the zero-field-cooled (ZFC) magnetic susceptibility $\chi(T) \equiv M(T)/H$ of SrMn_2Sb_2 in a small magnetic field $H = 0.1$ T applied in the ab plane (χ_{ab}) and along the c axis (χ_c). These data exhibit a clear AFM transition at $T_N = 110(5)$ K. The value of T_N is

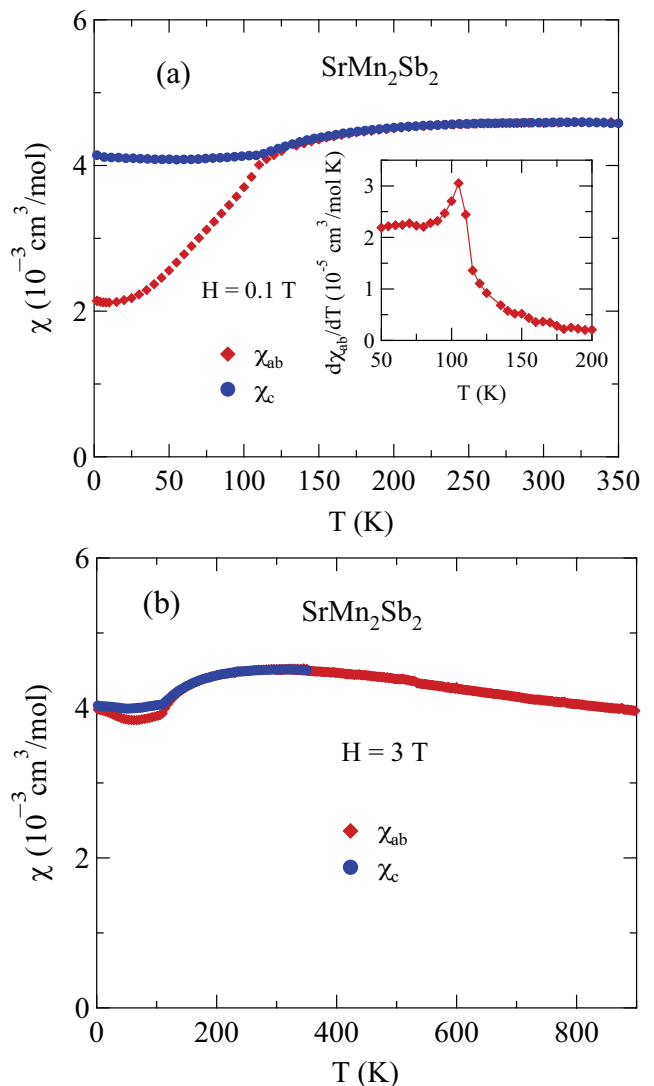


FIG. 4: (Color online) (a) Zero-field-cooled magnetic susceptibility χ of SrMn_2Sb_2 versus temperature T in a magnetic field $H = 0.1$ T applied in the ab plane (χ_{ab}) and along the c axis (χ_c). Inset: Derivative $d\chi_{ab}(T)/dT$ versus T for $H \parallel ab$ to identify T_N . (b) χ_{ab} and χ_c versus T for $1.8 \text{ K} \leq T \leq 900 \text{ K}$ measured in $H = 3$ T.

confirmed from a plot of $d\chi_{ab}(T)/dT$ versus T in the inset of Fig. 4(a). The anisotropy of χ below T_N indicates that the c axis is the hard axis and hence that the ordered moments lie in the ab plane. The substantial value of χ_{ab} for $T \rightarrow 0$ indicates that the AFM structure of SrMn_2Sb_2 could be either a collinear antiferromagnet with multiple domains aligned within the ab plane or an intrinsically noncollinear structure; this behavior is similar to that of the isostructural compound SrMn_2As_2 ³⁰ that was ultimately found to have a collinear AFM structure with the ordered moments aligned in the ab plane, but with three approximately equally-populated domains at an angle of 60° to each other which led to $\chi_{ab}(T \rightarrow 0) \approx \chi(T_N)/2$ ⁵¹, as also observed in Fig. 4(a).

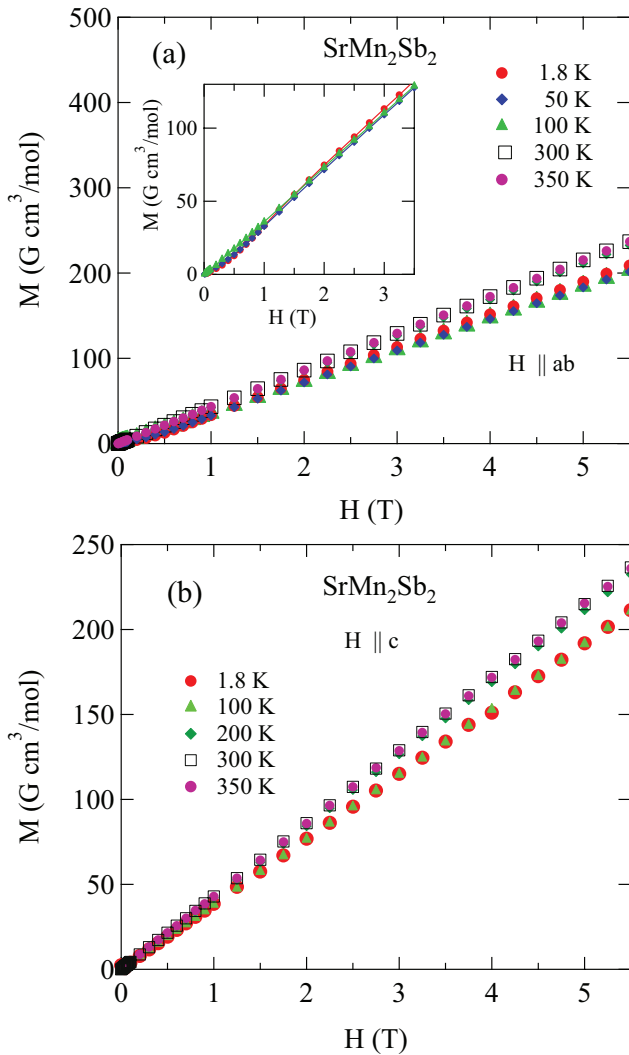


FIG. 5: (Color online) Magnetization M of SrMn_2Sb_2 as a function of magnetic field H at various temperatures T with (a) H in the ab plane ($H \parallel ab$) and (b) H along c axis ($H \parallel c$). The inset in (a) is an expanded plot of $M(H)$.

Figure 4(b) shows that the anisotropy in $\chi(T)$ almost disappears above T_N in a field of 3 T which indicates that the magnetocrystalline anisotropy in SrMn_2Sb_2 is rather small, as expected for Mn^{+2} with a d^5 electronic configuration and spin $S = 5/2$. These results also show that contrary to a three-dimensional antiferromagnet for which χ decreases above T_N , the data for SrMn_2Sb_2 increase above T_N , reach a broad maximum at ~ 300 K and then slowly decrease. A Curie-Weiss behavior is not attained up to 900 K, i.e., positive curvature in $\chi(T)$ is not clearly evident, indicating that strong dynamic AFM fluctuations occur up to at least 900 K. Within a local-moment picture, these features in $\chi(T)$ at $T > T_N$ are characteristic of a quasi-two-dimensional antiferromagnet.

$M(H)$ isotherms for a single crystal of SrMn_2Sb_2 with $H \parallel ab$ and $H \parallel c$ are shown in Figs. 5(a) and 5(b), re-

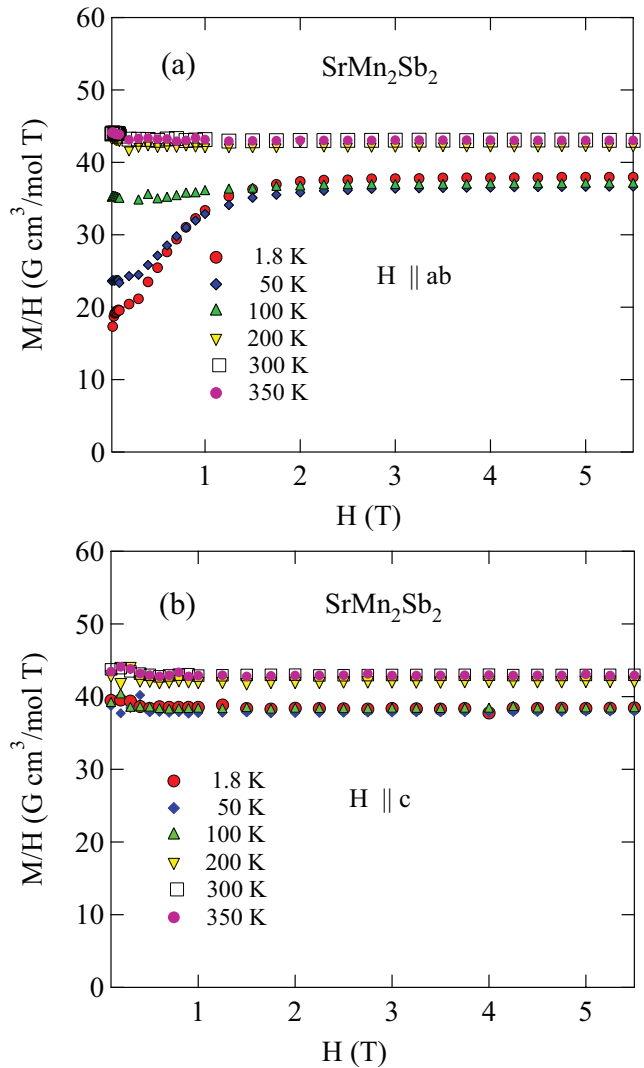


FIG. 6: (Color online) M/H versus H of SrMn_2Sb_2 at various listed temperatures T with (a) H in the ab plane ($H \parallel ab$) and (b) H along the c axis ($H \parallel c$). The data in (a) for $T = 1.8$ K and 50 K show a smooth metamagnetic transition that is spread out between $H = 0$ and $H = 1$ T.

spectively. The data for $H \parallel c$ are proportional to H at all temperatures, indicating lack of significant ferromagnetic or saturable paramagnetic impurities. However, for $H \parallel ab$, the magnetization shows *positive* curvature for $H \lesssim 1$ T at low temperatures. An expanded plot of the data with $H \leq 3$ T for $T = 100$ K and 1.8 K is shown in the inset of Fig. 5(a), where the positive curvature is somewhat more apparent. One can greatly amplify the low-field $M(H)$ behaviors of SrMn_2Sb_2 by plotting M/H versus H as shown for $H \parallel ab$ and $H \parallel c$ in Figs. 6(a) and 6(b), respectively. If $M_{ab} \propto H$ at low fields, the result would just be a horizontal line. Instead, one sees in Fig. 6(a) a strong increase in M_{ab}/H with increasing H up to 1 T, where it levels out. This indicates that a continuous ab -plane metamagnetic transition for $H \parallel ab$ with $0 < H \lesssim 1$ T occurs at low temperatures

$T \leq 50 \text{ K} < T_N$ but not at $T \gtrsim 100 \text{ K} \approx T_N$ or for $H \parallel c$ at all temperatures from 1.8 to 350 K. Thus this transition is associated with the AFM state. Determining the nature of this metamagnetic transition requires further investigation.

Our results disagree in two important ways with the $\chi(T)$ data for a polycrystalline sample of SrMn_2Sb_2 in Fig. 2 of Ref.⁶³. First, these authors reported a broad peak at $\sim 250 \text{ K}$ in $\chi(T)$ measured in 0.1 T which bears no resemblance to the powder average of the $\chi(T)$ data in $H = 0.1 \text{ T}$ in our Fig. 4(a). Second, the average of their data from $T = 5$ to 300 K is $\approx 0.05 \text{ cm}^3/\text{mole-SrMn}_2\text{Sb}_2$, whereas the value of the powder-averaged χ up to 300 K in our Fig. 4(a) is $\approx 4 \times 10^{-3} \text{ cm}^3/\text{mole-SrMn}_2\text{Sb}_2$, more than an order of magnitude smaller. We infer that their results were strongly affected by FM MnSb impurities which have a strongly composition-dependent Curie temperature T_C that can vary between 100 and 320 K^{70,71} and with a large ordered moment of $\sim 3 \mu_B/\text{Mn}$ ⁷⁰. We prevented the formation of MnSb impurities when growing our SrMn_2Sb_2 crystals by using excess Sr in the crystal growth, as noted in Sec. II.

The presence of FM MnAs impurities with $T_C = 317 \text{ K}$ in the early BaMn_2As_2 crystals made it tedious to obtain the intrinsic anisotropic $\chi(T)$ of this compound because the contribution of these impurities to the measured magnetization had to be accounted for by taking χ to be the high-field slope of an $M(H)$ isotherm that was measured at each temperature for each field direction²⁶. The small amount of MnAs impurities present in those crystals did not contribute significantly to the magnetization when the measurement temperature was above T_C of MnAs.

2. BaMn_2Sb_2

Plots of the the isothermal magnetization M of a BaMn_2Sb_2 single crystal versus H for $H \parallel ab$ and $H \parallel c$ at various temperatures are shown in Figs. 7(a) and 7(b), respectively. Anisotropic behavior between $H \parallel ab$ and $H \parallel c$ is evident at low temperatures. One sees from these plots that the contribution of ferromagnetic or saturable paramagnetic impurities to the magnetization data is insignificant at all measured temperatures.

The zero-field-cooled (ZFC) magnetic susceptibilities $\chi \equiv M/H$ of BaMn_2Sb_2 versus T from 1.8 to 550 K with $H = 3 \text{ T}$ applied along the c axis ($H \parallel c$, χ_c), and $\chi(T)$ for T for 1.8 to 900 K with $H = 3 \text{ T}$ applied in the ab plane ($H \parallel ab$, χ_{ab}), are shown in Fig. 8. The anisotropy between the c axis and ab plane data below $T_N = 450(10) \text{ K}$ is a textbook example of collinear long-range AFM ordering with the ordered moments oriented along the c axis^{72,73}. A more precise estimate of T_N is obtained from a plot of the derivative $d\chi_{ab}/dT$ versus T in the inset of Fig. 8. A clear peak in these data gives the same Néel temperature but with a smaller error bar, $T_N = 450(5) \text{ K}$.

Figure 8 further shows that $\chi_{ab}(T)$ does not decrease

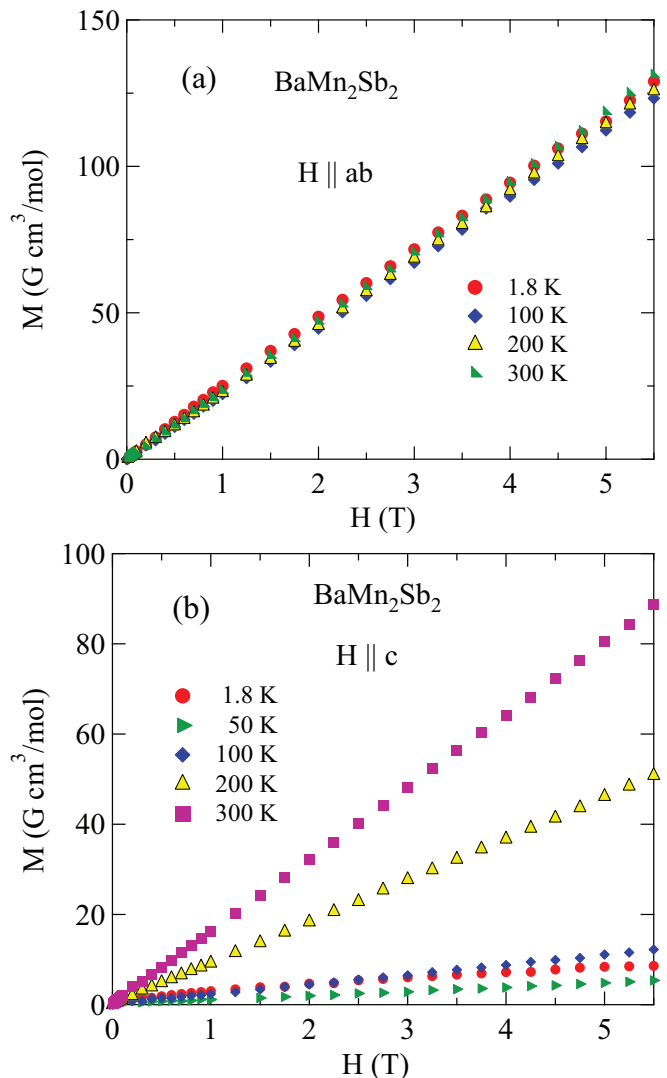


FIG. 7: (Color online) Isothermal magnetization M of BaMn_2Sb_2 as a function of magnetic field H at the temperatures listed with (a) H in the ab plane ($H \parallel ab$) and (b) H along the c axis ($H \parallel c$). Note the different scales on the ordinates in (a) and (b).

above T_N as would be expected for a three-dimensional antiferromagnet, but instead increases and appears to approach a maximum at $\sim 600 \text{ K}$, followed by a slow decrease. This paramagnetic behavior is similar to that of SrMn_2Sb_2 discussed above and is characteristic of strong short-range dynamic two-dimensional AFM fluctuations above T_N ⁵⁶ as seen previously in, e.g., tetragonal BaMn_2As_2 ⁵⁶ and trigonal CaMn_2As_2 and SrMn_2As_2 ³⁰.

Our overall $\chi(T)$ and $M(H)$ results for BaMn_2Sb_2 are similar to those for other isostructural Mn compounds such as BaMn_2As_2 ²⁶, BaMn_2P_2 ²⁵, $(\text{Ca,Ba})\text{Mn}_2\text{Ge}_2$ ⁷⁴, and BaMn_2Bi_2 ²⁹. Electronic structure studies of a G-type collinear AFM structure in BaMn_2Sb_2 were carried out previously and the ordered Mn moment at $T = 0$ was calculated to be $\approx 3.8 \mu_B/\text{Mn}$ ⁶¹ or $3.55 \mu_B/\text{Mn}$ ⁶².

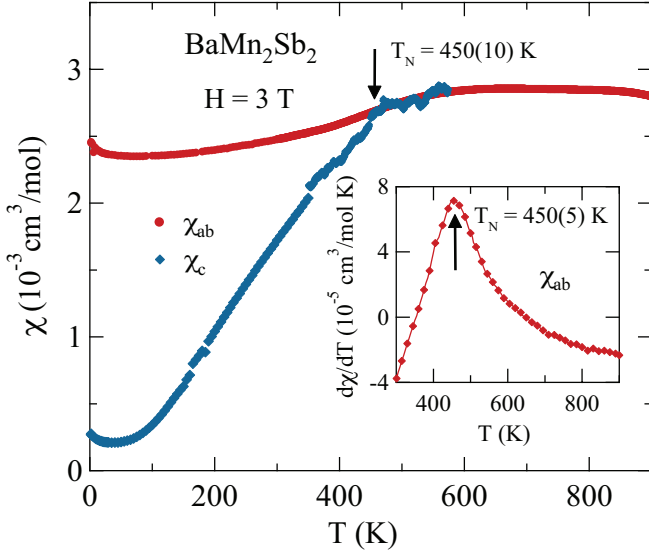


FIG. 8: (Color online) ZFC magnetic susceptibility $\chi(T)$ of BaMn_2Sb_2 as a function of temperature T for 1.8 to 550 K in $H = 3$ T applied along the c axis and $\chi(T)$ for $1.8 \text{ K} \leq T \leq 900 \text{ K}$ in $H = 3$ T applied in the ab plane. The T_N obtained from these data is $450(10)$ K. Inset: The derivative $d\chi_{ab}/dT$ versus T which was used to obtain another estimate $T_N = 450(5)$ K from the temperature of the peak.

D. Heat Capacity

The $C_p(T)$ data for BaMn_2Sb_2 and SrMn_2Sb_2 in the temperature range between 1.8 and 300 K are shown in Figs. 9(a) and 9(b), respectively. The temperature of the sharp λ -type anomaly in $C_p(T)$ for SrMn_2Sb_2 at 110 K is in good agreement with the T_N found from the above $\chi(T)$ data for this material. The insets in Figs. 9(a) and 9(b) show a linear C_p/T versus T^2 behavior for $1.8 \leq T \leq 5$ K. Hence we fit these data by the expression

$$\frac{C_p}{T} = \gamma + \beta T^2, \quad (2)$$

where the coefficient γ in metals is due to the conduction electron contribution (Sommerfeld coefficient) if nonzero and β reflects the low- T Debye T^3 lattice contribution together with a three-dimensional AFM spin-wave contribution if present. For BaMn_2Sb_2 , the fit yields

$$\gamma = 0.01(1) \text{ mJ/mol K}^2, \quad (3a)$$

$$\beta = 1.17(2) \text{ mJ/mol K}^4, \quad (3b)$$

and for SrMn_2Sb_2 we obtain

$$\gamma = 0.02(4) \text{ mJ/mol K}^2, \quad (4a)$$

$$\beta = 0.680(3) \text{ mJ/mol K}^4. \quad (4b)$$

The null values of γ are consistent with the insulating ground states found from the respective $\rho(T)$ measurements in Sec III B. Assuming no contribution from 3D AFM spin waves, we estimate the Debye temperatures

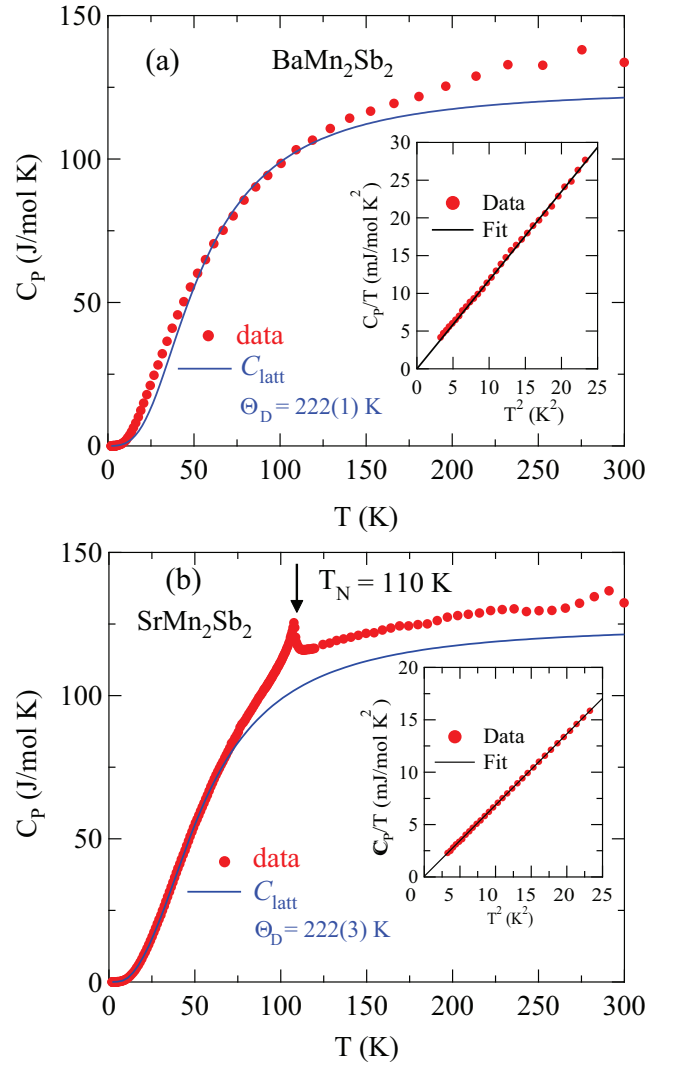


FIG. 9: (Color online) Heat capacity C_p versus temperature T and fits of $C_{\text{latt}}(T)$ in Eqs. (7) to the data over restricted temperature intervals (see text) for (a) BaMn_2Sb_2 and (b) SrMn_2Sb_2 . The fits and extrapolations are shown as blue curves, and the fitted Debye temperatures Θ_D are shown in each panel. The respective insets show $C_p(T)/T$ versus T^2 for $T < 5$ K, where the straight lines through the respective data are fits by Eq. (2) where the fitted parameters are given in Eqs. (3) and (4), respectively.

(Θ_D) of the two compounds from the β values using the expression

$$\Theta_D = \left(\frac{12\pi^4 R n}{5\beta} \right)^{1/3} \quad (5)$$

where R is the molar gas constant and n is the number of atoms per formula unit ($n = 5$ for BaMn_2Sb_2 and SrMn_2Sb_2). We thus obtain

$$\Theta_D = 202(1) \text{ K} \quad (\text{BaMn}_2\text{Sb}_2), \quad (6a)$$

$$= 242.5(3) \text{ K} \quad (\text{SrMn}_2\text{Sb}_2). \quad (6b)$$

The lattice contributions $C_{\text{latt}}(T)$ to $C_p(T)$ for BaMn_2Sb_2 and SrMn_2Sb_2 at higher temperatures were obtained by fitting the respective $C_p(T)$ data over specified temperature ranges where the magnetic contribution $C_{\text{mag}}(T)$ was expected to be small by the molar heat capacity expression

$$C_{\text{latt}} = n C_{V\text{Debye}}, \quad (7a)$$

where n is defined above. Here $C_{V\text{Debye}}$ is the Debye lattice heat capacity per mole of atoms given by

$$C_{V\text{Debye}}(T) = 9R \left(\frac{T}{\Theta_D} \right)^3 \int_0^{\Theta_D/T} \frac{x^4 e^x}{(e^x - 1)^2} dx, \quad (7b)$$

where Θ_D is the Debye temperature. An accurate analytic Padé approximant was used for the Debye function in Eq. (7b) for fitting the $C_p(T)$ data⁷⁵. The fit of $C_p(T)$ for BaMn_2Sb_2 by Eqs. (7) over the temperature range from 50 to 100 K and its extrapolation to higher temperatures is shown by the solid blue curve in Fig. 9(a), yielding $\Theta_D = 222(1)$ K. This value of Θ_D is comparable with the value of 202 K in Eq. (6a) determined from the fit of the C_p for BaMn_2Sb_2 at low T by Eq. (2).

For SrMn_2Sb_2 , the $C_p(T)$ data for $1.8 \leq T \leq 10$ K and $50 \leq T \leq 70$ K were fitted simultaneously by Eqs. (7). The fit and its interpolation and extrapolation are shown by the blue curve in Fig. 9(b) obtained using the fitted Debye temperature $\Theta_D = 222(3)$ K. Again, the value of Θ_D for SrMn_2Sb_2 is comparable with the value of 242.5 K in Eq. (6b) determined from the fit of the $C_p(T)$ data at low T by Eq. (2).

The fitted constant-volume $C_{\text{latt}}(T)$ in Fig. 9(b) is used to obtain an estimate of $C_{\text{mag}}(T)$ to the measured heat capacity of SrMn_2Sb_2 . The molar magnetic heat capacity is obtained from

$$C_{\text{mag}}(T) = C_p(T) - C_{\text{latt}}(T). \quad (8)$$

The $C_{\text{mag}}(T)$ for SrMn_2Sb_2 obtained is shown in Fig. 10(a), where a sharp peak at $T_N = 110$ K is seen. The small broad bump below T_N is an artifact and the nonzero C_{mag} above T_N indicates strong dynamic short-range AFM order above T_N .

It is well known that the heat capacity of a material at constant pressure C_p is larger than at constant volume C_v , and hence the $C_{\text{mag}}(T)$ in Fig. 10(a) obtained using Eqs. (7) would then be less than shown in the figure. This difference is given by the conventional expression

$$C_p - C_v = TV_M \frac{\alpha^2}{\kappa_T}, \quad (9)$$

where α is the volume thermal expansion coefficient, κ_T is the isothermal compressibility, and since C is normalized here per mole of compound, $V_M \approx 4.26 \times 10^{-5}$ m³/mol is the molar volume for SrMn_2Sb_2 . For the similar compound SrCo_2As_2 at $T \sim 200$ K, one has $\alpha = 2.4 \times 10^{-5}$ /K [13], and $\kappa_T \approx 0.0078$ GPa⁻¹ [76]. Using these values, Eq. (9) gives $C_p - C_v \approx 0.6$ J/mol K at 200 K, which is

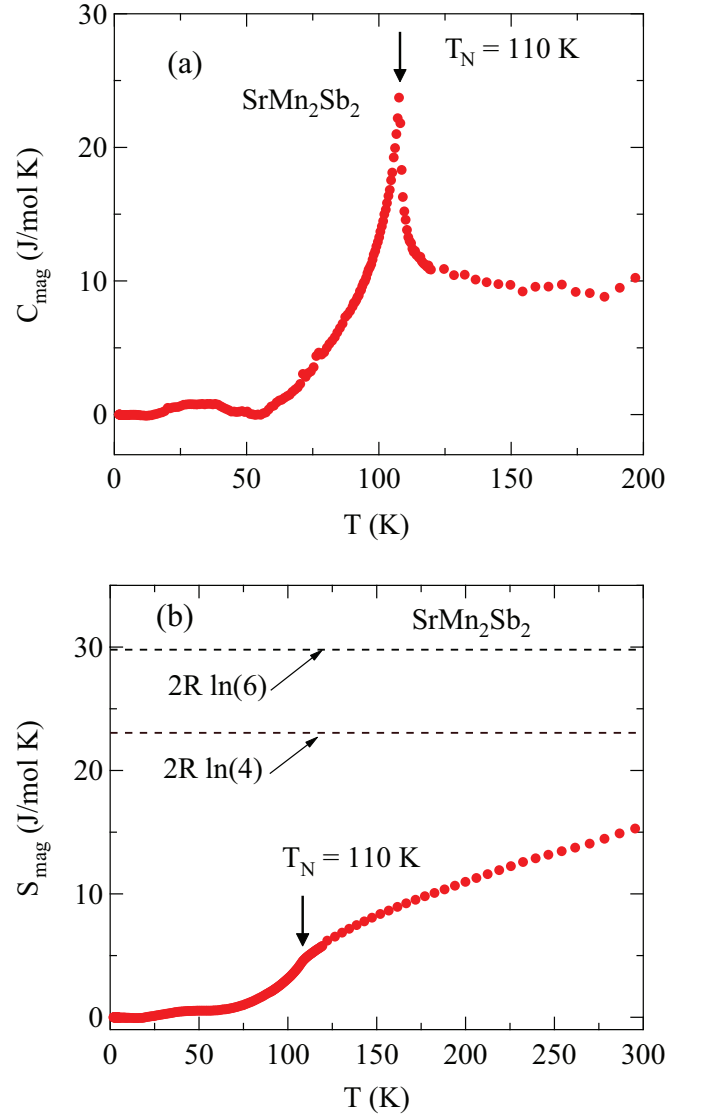


FIG. 10: (Color online) (a) Molar magnetic heat capacity C_{mag} versus temperature T for SrMn_2Sb_2 obtained using Eq. (8). The λ anomaly at $T_N = 110$ K arises from AFM order with the moments aligned in the ab plane. (b) Molar magnetic entropy $S_{\text{mag}}(T)$ of SrMn_2Sb_2 obtained using the data in (a) and Eq. (10). The dashed lines are $S_{\text{mag}}(T \rightarrow \infty)$ for $S = 5/2$ and $S = 3/2$ in Eqs. (11), as indicated.

only about 6% of $C_{\text{mag}}(200$ K) in Fig. 10(a). Hence we ignore this difference in the subsequent discussion.

The magnetic entropy $S_{\text{mag}}(T)$ for SrMn_2Sb_2 is calculated from $C_{\text{mag}}(T)$ in Fig. 10(a) using

$$S_{\text{mag}}(T) = \int_0^T \frac{C_{\text{mag}}(T)}{T} dT, \quad (10)$$

and the result is shown in Fig. 10(b). The entropy of completely disordered spins S per mole of SrMn_2Sb_2 is

$S(T \rightarrow \infty) = 2R \ln(2S + 1)$, which gives

$$S_{\text{mag}}(T \rightarrow \infty) = 23.1 \frac{\text{J}}{\text{mol K}} \quad (S = 3/2) \quad (11a)$$

$$= 29.8 \frac{\text{J}}{\text{mol K}} \quad (S = 5/2), \quad (11b)$$

as shown by the horizontal dashed black lines in Fig. 10(b). The $S_{\text{mag}}(300 \text{ K}) \approx 15 \text{ J/mol K}$ for SrMn_2Sb_2 in Fig. 10(b) is only $\approx 50\%$ of the value for $S = 5/2$ in Eqs. (11) and is still only $\approx 65\%$ of the value for $S = 3/2$. The remaining entropy is evidently not released until much higher temperatures. Thus the strong dynamic short-range AFM order revealed in the $C_{\text{mag}}(T)$ and $S_{\text{mag}}(T)$ data above T_N is consistent with the above conclusion from the $\chi(T)$ data that dynamic short-range AFM order survives from T_N up to at least 900 K.

IV. SUMMARY

Refinements of our x-ray diffraction data confirm that SrMn_2Sb_2 crystallizes in the trigonal CaAl_2Si_2 -type structure with space group $P\bar{3}m1$, whereas BaMn_2Sb_2 adopts the body-centered tetragonal ThCr_2Si_2 structure with space group $I4/mmm$. Heat capacity $C_p(T)$ and electrical resistivity $\rho(T)$ measurements indicate that both compounds are insulators at low temperatures. At higher temperatures, the $\rho(T)$ data show that SrMn_2Sb_2 and BaMn_2Sb_2 are semiconductors with activation energies estimated to be $\gtrsim 0.35$ and 0.16 eV , respectively.

Long-range antiferromagnetic (AFM) order arising from the nominal Mn^{+2} spins with d^5 electronic configuration and spin $S = 5/2$ is reported for single crystals of SrMn_2Sb_2 and BaMn_2Sb_2 at $T_N = 110 \text{ K}$ and 450 K , respectively, as determined from magnetic susceptibility $\chi(T)$ and $C_p(T)$ measurements. We infer from the anisotropy in the $\chi(T)$ data below T_N that the ordered moments in SrMn_2Sb_2 lie in the ab plane and exhibit either intrinsic planar noncollinear AFM order or extrinsic noncollinear AFM order arising from multiple collinear AFM ab -plane domains. From magnetization versus field isotherms, we discovered that SrMn_2Sb_2 exhibits a continuous metamagnetic transition at low fields between 0 and 1 T. The nature of this transition remains to be

determined. On the other hand, the classic anisotropy of the $\chi(T)$ data for BaMn_2Sb_2 at temperatures below T_N indicates that this compound exhibits collinear AFM order with the moments aligned along the c axis.

The $\chi(T)$ above T_N in SrMn_2Sb_2 is isotropic for both SrMn_2Sb_2 and BaMn_2Sb_2 , indicating weak magnetocrystalline anisotropy. Both compounds exhibit broad maxima in $\chi(T)$ above T_N as shown in Figs. 4(b) and 8, respectively, and do not settle into a Curie-Weiss behavior up to 900 K. Furthermore, the magnetic entropy of SrMn_2Sb_2 obtained at 300 K from the heat capacity measurements is only half that expected for disordered Mn^{+2} spins $S = 5/2$. These results indicate that within a local-moment picture, SrMn_2Sb_2 and BaMn_2Sb_2 exhibit strong dynamic AFM fluctuations up to at least 900 K and hence are quasi-two-dimensional (2D) local-moment antiferromagnets⁵⁶.

The differences between the smaller intraplanar and larger interplanar interatomic distances between Mn atoms in Table II and the resultant differences between their interactions in SrMn_2Sb_2 and BaMn_2Sb_2 are expected to strongly influence their magnetic properties. In both compounds, the smallest intraplanar distances between the Mn atoms are much smaller than the smallest interlayer distances. This apparently leads to the 2D dynamic short-range correlations in SrMn_2Sb_2 and BaMn_2Sb_2 above T_N . The differences in the structures of the Mn layers in SrMn_2Sb_2 and BaMn_2Sb_2 also appear to be important. From Table I, these differences may contribute to the large differences in Néel temperatures of layered Mn pnictides between the CaAl_2Si_2 and ThCr_2Si_2 crystal structures. Theoretical studies of the origins of these behaviors would be most interesting.

Acknowledgments

We thank Yogesh Singh for helpful correspondence. The research in Ames was supported by the U.S. Department of Energy, Office of Basic Energy Sciences, Division of Materials Sciences and Engineering. Ames Laboratory is operated for the U.S. Department of Energy by Iowa State University under Contract No. DE-AC02-07CH11358.

¹ Y. Kamihara, T. Watanabe, M. Hirano, and H. Hosono, Iron-Based Layered Superconductors $\text{La}(\text{O}_{1-x}\text{F}_x)\text{FeAs}$ ($x = 0.05\text{--}0.12$) with $T_c = 26 \text{ K}$, *J. Am. Chem. Soc.* **130**, 3296 (2008).

² G. Just and P. Paufler, On the coordination of ThCr_2Si_2 (BaAl_4)-type compounds within the field of free parameters, *J. Alloys Compd.* **232**, 1 (1996).

³ D. C. Johnston, The puzzle of high temperature superconductivity in layered iron pnictides and chalcogenides, *Adv. Phys.* **59**, 803 (2010).

⁴ G. R. Stewart, Superconductivity in iron compounds, *Rev. Mod. Phys.* **83**, 1589 (2011).

⁵ D. J. Scalapino, A common thread: The pairing interaction for unconventional superconductors, *Rev. Mod. Phys.* **84**, 1383 (2012).

⁶ C. Wang, L. Li, S. Chi, Z. Zhu, Z. Ren, Y. Li, Y. Wang, X. Lin, Y. Luo, S. Jiang, X. Xu, G. Cao, and Z. Xu, Thorium-doping-induced superconductivity up to 56 K in $\text{Gd}_{1-x}\text{Th}_x\text{FeAsO}$, *Europhys. Lett.* **83**, 67006 (2008).

⁷ A. S. Sefat, D. J. Singh, R. Jin, M. A. McGuire, B. C. Sales,

- and D. Mandrus, Renormalized behavior and proximity of BaCo_2As_2 to a magnetic quantum critical point, *Phys. Rev. B* **79**, 024512 (2009).
- ⁸ H. Ohta and K. Yoshimura, Anomalous magnetization in the layered itinerant ferromagnet LaCoAsO , *Phys. Rev. B* **79**, 184407 (2009).
 - ⁹ B. Cheng, B. F. Hu, R. H. Yuan, T. Dong, A. F. Fang, Z. G. Chen, G. Xu, Y. G. Shi, P. Zheng, J. L. Luo, and N. L. Wang, Field-induced spin-flop transitions in single-crystalline CaCo_2As_2 , *Phys. Rev. B* **85**, 144426 (2012).
 - ¹⁰ D. G. Quirinale, V. K. Anand, M. G. Kim, A. Pandey, A. Huq, P. W. Stephens, T. W. Heitmann, A. Kreyssig, R. J. McQueeney, D. C. Johnston, and A. I. Goldman, Crystal and magnetic structure of $\text{CaCo}_{1.86}\text{As}_2$ studied by x-ray and neutron diffraction, *Phys. Rev. B* **88**, 174420 (2013).
 - ¹¹ V. K. Anand, R. S. Dhaka, Y. Lee, B. N. Harmon, A. Kaminski, and D. C. Johnston, Physical properties of metallic antiferromagnetic $\text{CaCo}_{1.86}\text{As}_2$, *Phys. Rev. B* **89**, 214409 (2014).
 - ¹² V. K. Anand, D. G. Quirinale, Y. Lee, B. N. Harmon, Y. Furukawa, V. V. Ogloblichev, A. Huq, D. L. Abernathy, P. W. Stephens, R. J. McQueeney, A. Kreyssig, A. I. Goldman, and D. C. Johnston, Crystallography and physical properties of BaCo_2As_2 , $\text{Ba}_{0.94}\text{K}_{0.06}\text{Co}_2\text{As}_2$ and $\text{Ba}_{0.78}\text{K}_{0.22}\text{Co}_2\text{As}_2$, *Phys. Rev. B* **90**, 064517 (2014).
 - ¹³ A. Pandey, D. G. Quirinale, W. Jayasekara, A. Sapkota, M. G. Kim, R. S. Dhaka, Y. Lee, T. W. Heitmann, P. W. Stephens, V. Ogloblichev, A. Kreyssig, R. J. McQueeney, A. I. Goldman, A. Kaminski, B. N. Harmon, Y. Furukawa, and D. C. Johnston, Crystallographic, electronic, thermal, and magnetic properties of single-crystal SrCo_2As_2 , *Phys. Rev. B* **88**, 014526 (2013).
 - ¹⁴ W. Jayasekara, Y. Lee, A. Pandey, G. S. Tucker, A. Sapkota, J. Lamsal, S. Calder, D. L. Abernathy, J. L. Niedziela, B. N. Harmon, A. Kreyssig, D. Vaknin, D. C. Johnston, A. I. Goldman, and R. J. McQueeney, Stripe Antiferromagnetic Spin Fluctuations in SrCo_2As_2 , *Phys. Rev. Lett.* **111**, 157001 (2013).
 - ¹⁵ N. S. Sangeetha, E. Cuervo-Reyes, A. Pandey, and D. C. Johnston, EuCo_2P_2 : A model molecular-field helical Heisenberg antiferromagnet, *Phys. Rev. B* **94**, 014422 (2016).
 - ¹⁶ S.-W. Park, H. Mizoguchi, K. Kodama, S.-I. Shamoto, T. Otomo, S. Matsuishi, T. Kamiya, and H. Hosono, Magnetic Structure and Electromagnetic Properties of LnCrAsO with a ZrCuSiAs -type Structure ($\text{Ln} = \text{La}, \text{Ce}, \text{Pr}, \text{and Nd}$), *Inorg. Chem.* **52**, 13363 (2013).
 - ¹⁷ D. J. Singh, A. S. Sefat, M. A. McGuire, B. C. Sales, D. Mandrus, L. H. VanBebber, and V. Keppens, Itinerant antiferromagnetism in BaCr_2As_2 : Experimental characterization and electronic structure calculations, *Phys. Rev. B* **79**, 094429 (2009).
 - ¹⁸ K. A. Filsinger, W. Schnelle, P. Adler, G. H. Fecher, M. Reehuis, A. Hoser, J.-U. Homann, P. Werner, M. Greenblatt, and C. Felser, Antiferromagnetic structure and electronic properties of BaCr_2As_2 and BaCrFeAs_2 , *Phys. Rev. B* **95**, 184414 (2017).
 - ¹⁹ P. G. Naumov, K. Filsinger, O. I. Barkalov, G. H. Fecher, S. A. Medvedev, and C. Felser, Pressure-induced transition to the collapsed tetragonal phase in BaCr_2As_2 , *Phys. Rev. B* **95**, 144106 (2017).
 - ²⁰ P. Richard, A. van Roekeghem, B. Q. Lv, T. Qian, T. K. Kim, M. Hoesch, J.-P. Hu, A. S. Sefat, S. Biermann, and H. Ding, Is BaCr_2As_2 symmetrical to BaFe_2As_2 with respect to half $3d$ shell filling?, *Phys. Rev. B* **95**, 184516 (2017).
 - ²¹ U. B. Paramanik, R. Prasad, C. Geibel, and Z. Hossain, Itinerant and local-moment magnetism in EuCr_2As_2 single crystals, *Phys. Rev. B* **89**, 144423 (2014).
 - ²² M. Pfisterer and G. Nagorsen, On the Structure of Ternary Arsenides, *Z. Naturforsch.* **35b**, 703 (1980).
 - ²³ M. Pfisterer and G. Nagorsen, Bonding and Magnetic Properties in Ternary Arsenides ET_2As_2 , *Z. Naturforsch.* **38b**, 811 (1983).
 - ²⁴ P. Das, N. S. Sangeetha, G. R. Lindemann, T. W. Heitmann, A. Kreyssig, A. I. Goldman, R. J. McQueeney, D. C. Johnston, and D. Vaknin, Itinerant G-type antiferromagnetic order in SrCr_2As_2 , *Phys. Rev. B* **96**, 014411 (2017).
 - ²⁵ S. L. Brock, J. E. Greedan, and S. M. Kauzlarich, Resistivity and Magnetism of AMn_2P_2 ($A = \text{Sr}, \text{Ba}$): The Effect of Structure Type on Physical Properties, *J. Solid State Chem.* **113**, 303 (1994).
 - ²⁶ Y. Singh, A. Ellern, and D. C. Johnston, Magnetic, transport and thermal properties of single crystals of the layered arsenide BaMn_2As_2 , *Phys. Rev. B* **79**, 094519 (2009).
 - ²⁷ Z. W. Wang, H. X. Yang, H. F. Tian, H. L. Shi, J. B. Lu, Y. B. Qin, Z. Wang, and J. Q. Li, Structural and physical properties of SrMn_2As_2 , *J. Phys. Chem. Solids* **72**, 457 (2011).
 - ²⁸ H. F. Wang, K. F. Cai, L. Wang, C. W. Zhou, Synthesis and thermoelectric properties of BaMn_2Sb_2 single crystals, *J. Alloys Compd.* **477**, 519 (2009).
 - ²⁹ B. Saparov and A. S. Sefat, Crystals, magnetic and electronic properties of a new ThCr_2Si_2 -type BaMn_2Bi_2 and K-doped compositions, *J. Solid State Chem.* **204**, 32 (2013).
 - ³⁰ N. S. Sangeetha, A. Pandey, Z. A. Benson and D. C. Johnston, Strong magnetic correlations to 900 K in single crystals of the trigonal antiferromagnetic insulators SrMn_2As_2 and CaMn_2As_2 , *Phys. Rev. B* **94**, 094417 (2016).
 - ³¹ H. Yanagi, T. Watanabe, K. Kodama, S. Iikubo, S. Shamoto, T. Kamiya, M. Hirano, and H. Hosono, Antiferromagnetic bipolar semiconductor LaMnPO with ZrCuSiAs -type structure, *J. Appl. Phys.* **105**, 093916 (2009).
 - ³² M. A. McGuire and V. O. Garlea, Short- and long-range magnetic order in LaMnAsO , *Phys. Rev. B* **93**, 054404 (2016).
 - ³³ Q. Zhang, C. M. N. Kumar, W. Tian, K. W. Dennis, A. I. Goldman, and D. Vaknin, Structure and magnetic properties of LnMnSbO ($\text{Ln} = \text{La}, \text{Ce}$), *Phys. Rev. B* **93**, 094413 (2016).
 - ³⁴ Y. Li, Y. Luo, L. Li, B. Chen, X. Xu, J. Dai, X. Yang, L. Zhang, G. Cao, and Z. Xu, Kramers non-magnetic superconductivity in LnNiAsO superconductors, *J. Phys.: Condens. Matter* **26**, 425701 (2014).
 - ³⁵ M. Tegel, D. Bichler, and D. Johrendt, Synthesis, crystal structure and superconductivity of LaNiPO , *Solid State Sciences* **10**, 193 (2008).
 - ³⁶ F. Ronning, N. Kurita, E. D. Bauer, B. L. Scott, T. Park, T. Klimczuk, R. Movshovich, and J. D. Thompson, The first order phase transition and superconductivity in BaNi_2As_2 single crystals, *J. Phys.: Condens. Matter* **20**, 342203 (2008).
 - ³⁷ E. D. Bauer, F. Ronning, B. L. Scott, and J. D. Thompson, Superconductivity in SrNi_2As_2 single crystals, *Phys. Rev. B* **78**, 172504 (2008).
 - ³⁸ J. W. Simonson, Z. P. Yin, M. Pezzoli, J. Guo, J. Liu, K. Post, A. Efimenko, N. Hollmann, Z. Hu, H.-J. Lin, C.-T.

- Chen, C. Marques, V. Leyva, G. Smith, J. W. Lynn, L. L. Sun, G. Kotliar, D. N. Basov, L. H. Tjeng, and M. C. Aronson, From antiferromagnetic insulator to correlated metal in pressurized and doped LaMnPO, *Proc. Nat. Acad. Sci.* **109**, E1815 (2012).
- ³⁹ J. W. Simonson, K. Post, C. Marques, G. Smith, O. Khatib, D. N. Basov, and M. C. Aronson, Gap states in insulating LaMnPO_{1-x}F_x ($x = 0-0.3$), *Phys. Rev. B* **84**, 165129 (2011).
- ⁴⁰ Y.-L. Sun, J.-K. Bao, Y.-K. Luo, C.-M. Feng, Z.-A. Xu, and G.-H. Cao, Insulator-to-metal transition and large thermoelectric effect in La_{1-x}Sr_xMnAsO, *Europhys. Lett.* **98**, 17009 (2012).
- ⁴¹ T. Hanna, S. Matsuishi, K. Kodama, T. Otomo, S.-I. Shamoto, and H. Hosono, From antiferromagnetic insulator to ferromagnetic metal: Effects of hydrogen substitution in LaMnAsO, *Phys. Rev. B* **87**, 020401(R) (2013).
- ⁴² Y. Singh, M. A. Green, Q. Huang, A. Kreyssig, R. J. McQueeney, D. C. Johnston, and A. I. Goldman, Magnetic order in BaMn₂As₂ from neutron diffraction measurements, *Phys. Rev. B* **80**, 100403(R) (2009).
- ⁴³ S. Calder, B. Sagarov, H. B. Cao, J. L. Niedziela, M. D. Lumsden, A. S. Sefat, and A. D. Christianson, Magnetic structure and spin excitations in BaMn₂Bi₂, *Phys. Rev. B* **89**, 064417 (2014).
- ⁴⁴ A. T. Satya, A. Mani, A. Arulraj, N. V. Chandra Shekar, K. Vinod, C. S. Sundar, and A. Bharathi, Pressure-induced metallization of BaMn₂As₂, *Phys. Rev. B* **84**, 180515(R) (2011).
- ⁴⁵ A. Pandey, R. S. Dhaka, J. Lamsal, Y. Lee, V. K. Anand, A. Kreyssig, T. W. Heitmann, R. J. McQueeney, A. I. Goldman, B. N. Harmon, A. Kaminski, and D. C. Johnston, Ba_{1-x}K_xMn₂As₂: An Antiferromagnetic Local-Moment Metal, *Phys. Rev. Lett.* **108**, 087005 (2012).
- ⁴⁶ J.-K. Bao, H. Jiang, Y.-L. Sun, W.-H. Jiao, C.-Y. Shen, H.-J. Guo, Y. Chen, C.-M. Feng, H.-Q. Yuan, Z.-A. Xu, G.-H. Cao, R. Sasaki, T. Tanaka, K. Matsubayashi, and Y. Uwatoko, Weakly ferromagnetic metallic state in heavily doped Ba_{1-x}K_xMn₂As₂, *Phys. Rev. B* **85**, 144523 (2012).
- ⁴⁷ A. Pandey, B. G. Ueland, S. Yeninas, A. Kreyssig, A. Sapkota, Y. Zhao, J. S. Helton, J. W. Lynn, R. J. McQueeney, Y. Furukawa, A. I. Goldman, and D. C. Johnston, Coexistence of Half-Metallic Itinerant Ferromagnetism with Local-Moment Antiferromagnetism in Ba_{0.6}K_{0.4}Mn₂As₂, *Phys. Rev. Lett.* **111**, 047001 (2013).
- ⁴⁸ A. Pandey and D. C. Johnston, Ba_{0.4}Rb_{0.6}Mn₂As₂: A prototype half-metallic ferromagnet, *Phys. Rev. B* **92**, 174401 (2015).
- ⁴⁹ B. G. Ueland, A. Pandey, Y. Lee, A. Sapkota, Y. Choi, D. Haskel, R. A. Rosenberg, J. C. Lang, B. N. Harmon, D. C. Johnston, A. Kreyssig, and A. I. Goldman, Itinerant Ferromagnetism in the As 4*p* Conduction Band of Ba_{0.6}K_{0.4}Mn₂As₂ Identified by X-ray Magnetic Circular Dichroism, *Phys. Rev. Lett.* **114**, 217001 (2015).
- ⁵⁰ J. Lamsal, G. S. Tucker, T. W. Heitmann, A. Kreyssig, A. Jesche, A. Pandey, W. Tian, R. J. McQueeney, D. C. Johnston, and A. I. Goldman, Persistence of local-moment antiferromagnetic order in Ba_{1-x}K_xMn₂As₂, *Phys. Rev. B* **87**, 144418 (2013).
- ⁵¹ P. Das, N. S. Sangeetha, A. Pandey, Z. A. Benson, T. W. Heitmann, D. C. Johnston, A. I. Goldman, and A. Kreyssig, Collinear antiferromagnetism in trigonal SrMn₂As₂ revealed by single-crystal neutron diffraction, *J. Phys.: Condens. Matter* **29**, 035802 (2017).
- ⁵² C. A. Bridges, V. V. Krishnamurthy, S. Poulton, M. P. Paranthaman, B. C. Sales, C. Myers, and S. Bobev, Magnetic order in CaMn₂Sb₂ studied via powder neutron diffraction, *J. Magn. Magn. Mater.* **321**, 3653 (2009).
- ⁵³ W. Ratcliff II, A. L. Lima Sharma, A. M. Gomes, J. L. Gonzalez, Q. Huang, and J. Singleton, The magnetic ground state of CaMn₂Sb₂, *J. Magn. Magn. Mater.* **321**, 2612 (2009).
- ⁵⁴ J. W. Simonson, G. J. Smith, K. Post, M. Pezzoli, J. J. Kistner-Morris, D. E. McNally, J. E. Hassinger, C. S. Nelson, G. Kotliar, D. N. Basov, and M. C. Aronson, Magnetic and structural phase diagram of CaMn₂Sb₂, *Phys. Rev. B* **86**, 184430 (2012).
- ⁵⁵ Q. D. Gibson, H. Wu, T. Liang, M. N. Ali, N. P. Ong, Q. Huang, and R. J. Cava, Magnetic and electronic properties of CaMn₂Bi₂: A possible hybridization gap semiconductor, *Phys. Rev. B* **91**, 085128 (2015).
- ⁵⁶ D. C. Johnston, R. J. McQueeney, B. Lake, A. Honecker, M. E. Zhitomirsky, R. Nath, Y. Furukawa, V. P. Antropov, and Y. Singh, Magnetic exchange interactions in BaMn₂As₂: A case study of the J_1 - J_2 - J_c Heisenberg model, *Phys. Rev. B* **84**, 094445 (2011).
- ⁵⁷ D. E. McNally, J. W. Simonson, J. J. Kistner-Morris, G. J. Smith, J. E. Hassinger, L. DeBeer-Schmitt, A. I. Kolesnikov, I. A. Zaliznyak, and M. C. Aronson, CaMn₂Sb₂: Spin waves on a frustrated antiferromagnetic honeycomb lattice, *Phys. Rev. B* **91**, 180407(R) (2015).
- ⁵⁸ W. Xie, M. J. Winiarski, T. Klimczuk, and R. J. Cava, A tetragonal polymorph of SrMn₂P₂ made under high pressure—theory and experiment in harmony, *Dalton Trans.* **46**, 6835 (2017).
- ⁵⁹ E. Brechtel, G. Cordier, and H. Schäfer, Preparation and Crystal Structure of BaMn₂Sb₂, BaZn₂Sb₂ and BaCd₂Sb₂, *Z. Naturforsch.* **34b**, 921 (1979).
- ⁶⁰ G. Cordier and H. Schaefer, New intermetallic compounds in the anti-dicerium dioxide sulfide structure type, *Z. Naturforsch.* **31b**, 1459 (1976).
- ⁶¹ S.-Q. Xia, C. Myers, and S. Bobev, Combined Experimental and Density Functional Theory Studies on the Crystal Structures and Magnetic Properties of Mg(Mg_{1-x}Mn_x)₂Sb₂ ($x \approx 0.25$) and BaMn₂Sb₂, *Eur. J. Inorg. Chem.* **27**, 4262 (2008).
- ⁶² J. An, A. S. Sefat, D. J. Singh, and M.-H. Du, Electronic structure and magnetism in BaMn₂As₂ and BaMn₂Sb₂, *Phys. Rev. B* **79**, 075120 (2009).
- ⁶³ S. Bobev, J. Merz, A. Lima, V. Fritsch, J. D. Thompson, J. L. Sarrao, M. Gillissen, and R. Dronskowski, Unusual Mn–Mn Spin Coupling in the Polar Intermetallic Compounds CaMn₂Sb₂ and SrMn₂Sb₂, *Inorg. Chem.* **45**, 4047 (2006).
- ⁶⁴ J. Rodríguez-Carvajal, *Physica B* **192**, 55 (1993).
- ⁶⁵ APEX3, Bruker AXS Inc., Madison, Wisconsin, USA, 2015.
- ⁶⁶ SAINT, Bruker AXS Inc., Madison, Wisconsin, USA, 2015.
- ⁶⁷ L. Krause, R. Herbst-Irmer, G. M. Sheldrick, and D. J. Stalke, *Appl. Crystallogr.* **48**, 3 (2015).
- ⁶⁸ G. M. Sheldrick, SHELTX—Integrated space-group and crystal-structure determination, *Acta Crystallogr. A* **71**, 3 (2015).
- ⁶⁹ G. M. Sheldrick, Crystal structure refinement with SHELXL, *Acta Crystallogr. C* **71**, 3 (2015).
- ⁷⁰ T. Okita and Y. Makino, Crystal Magnetic Anisotropy and Magnetization of MnSb, *J. Phys. Soc. Jpn.* **25**, 120 (1968).
- ⁷¹ T. Chen, G. B. Charlan, and R. C. Keezer, Growth of MnSb Single Crystals by Puling with a Seed from Non-

- stoichiometric Molten Solution, *J. Cryst. Growth* **37**, 29 (1977).
- ⁷² D. C. Johnston, Magnetic Susceptibility of Collinear and Noncollinear Heisenberg Antiferromagnets, *Phys. Rev. Lett.* **109**, 077201 (2012).
- ⁷³ D. C. Johnston, Unified molecular field theory for collinear and noncollinear Heisenberg antiferromagnets, *Phys. Rev. B* **91**, 064427 (2015).
- ⁷⁴ B. Malaman, G. Venturini, R. Welter, and E. Ressouche, Neutron diffraction studies of CaMn_2Ge_2 and BaMn_2Ge_2 compounds: first examples of antiferromagnetic Mn planes in ThCr_2Si_2 -type structure compounds, *J. Alloys Compd.* **210**, 209 (1994).
- ⁷⁵ R. J. Goetsch, V. K. Anand, A. Pandey, and D. C. Johnston, Structural, thermal, magnetic, and electronic transport properties of the $\text{LaNi}_2(\text{Ge}_{1-x}\text{P}_x)_2$ system, *Phys. Rev. B* **85**, 054517 (2012).
- ⁷⁶ W. T. Jayasekara, U. S. Kaluarachchi, B. G. Ueland, A. Pandey, Y. B. Lee, V. Taufour, A. Sapkota, K. Kothapalli, N. S. Sangeetha, G. Fabbris, L. S. I. Veiga, Y. Feng, A. M. dos Santos, S. L. Bud'ko, B. N. Harmon, P. C. Canfield, D. C. Johnston, A. Kreyssig, and A. I. Goldman, Pressure-induced collapsed-tetragonal phase in SrCo_2As_2 , *Phys. Rev. B* **92**, 224103 (2015).